



HAL
open science

Landing Gear Noise Identification Using Phased Array with Experimental and Computational Data

Jean Bulté, Stéphane Redonnet

► **To cite this version:**

Jean Bulté, Stéphane Redonnet. Landing Gear Noise Identification Using Phased Array with Experimental and Computational Data. *AIAA Journal*, 2017, 55 (11), p. 3839 - 3850. 10.2514/1.J055643 . hal-01635430

HAL Id: hal-01635430

<https://hal.science/hal-01635430>

Submitted on 15 Nov 2017

HAL is a multi-disciplinary open access archive for the deposit and dissemination of scientific research documents, whether they are published or not. The documents may come from teaching and research institutions in France or abroad, or from public or private research centers.

L'archive ouverte pluridisciplinaire **HAL**, est destinée au dépôt et à la diffusion de documents scientifiques de niveau recherche, publiés ou non, émanant des établissements d'enseignement et de recherche français ou étrangers, des laboratoires publics ou privés.

Landing Gear Noise Identification Using Phased Array with Experimental and Computational Data

Jean Bulté* and Stéphane Redonnet†

ONERA—The French Aerospace Lab, F-92322 Châtillon, France

DOI: 10.2514/1.J055643

In regard to aircraft noise mitigation, this paper focuses on noise emission by a simplified nose landing gear (NLG), whose noise sources are identified by the means of sensor array methods. More precisely, following a former characterization of the aeroacoustics by the NLG via dedicated experiments and computations, the subsequent experimental and numerical noise signals are applied two popular sensor array methods of noise localization, namely, classical beam forming (CBF) and deconvolution approach for the mapping of acoustic sources (DAMAS). The resulting noise source maps are then analyzed from both the points of view of phenomenology (NLG noise generation mechanisms) and methodology (noise localization methods and application). The results show how sensor array methods (more especially DAMAS) are capable of revealing the underlying physics of the NLG noise source mechanisms, whether it is within an experimental or a computational context. This speaks in favor of a more systematic use of sensor array methods for investigating the noise physics of aircraft components.

I. Introduction

NOISE annoyance by aircraft is now officially identified as the major obstacle to sustainable air traffic growth. Therefore, all stakeholders involved in the development of aircraft systems or components are now focusing on practical ways (e.g., technological breakthroughs) to reduce the acoustic signature left by their products (see Fig. 1). This requires first mastering the noise phenomena that may occur in realistic situations, which generally implies deploying important research efforts, whether it is from a theoretical, an experimental, or a computational point of view. Because acoustics is a complex discipline, part of such efforts is devoted to the continuous development of advanced techniques, which are mandatory for noise physics to be measured, simulated, and/or analyzed still better.

The noise signature of aircraft includes two main contributions, respectively of propulsive and nonpropulsive origins. The first one, namely, the engine noise, is due to all engine propulsive devices (turbofan or turboprop), whereas the second one, namely, the airframe noise, is induced by the airframe and its appendages (fuselage, wings, slats, flaps, landing gears, cavities, etc.). Although the engine noise accounts for a dominant portion of the overall aircraft noise during take-off, the airframe noise component becomes equally important during the approach for landing, when the engine thrust is considerably reduced. In particular, a major airframe noise source on large transport aircraft is generated by landing gears, whose number and size are constantly increased (e.g., the A380; see Fig. 1).

The underlying mechanisms of noise emissions by landing gears are complex, as shown by various efforts to characterize them via experimentation [1–10] and/or numerical simulation [11–18]. In particular, some of these past experimental and numerical efforts offered a ground for the present work, which constitutes a step further toward the characterization of the aeroacoustics by landing gears. More precisely, here, we aimed at 1) identifying the noise sources of an in-flight nose landing gear (NLG) and 2) assessing how well noise

source localization methods based on sensor array techniques could be transposed from an experimental to a computational context. Indeed, the latter methods were originally developed—and are now widely used—for experimental purposes, whether it is regarding facility testing [4,6,19–21], fly-over [22–27], or in-flight [28,29] experiments. However, these array methods strongly rely on advanced signal processing techniques, whose performances may greatly vary depending on the configuration to be considered (e.g., array geometry employed, frequency range targeted, acoustic signal recorded) because of the possibly ill-posed nature of the associated inverse problem. In particular, there are legitimate concerns about the variability of a given array method upon the nature of the noise signal it is fed with, depending on whether such signal is of long duration but contaminated with extra noises (as generally happens with experiments) or is highly accurate but of very short duration (as usually happens with computations). In addition, among the various existing array methods, some of them are less accurate but more robust (e.g., classical beam forming, CBF), whereas others are of higher accuracy but come with a greater sensitivity (e.g., deconvolution approach for the mapping of acoustic sources, DAMAS).

Therefore, we here applied both CBF and DAMAS to either experimental or numerical databases from a former characterization of the aeroacoustics by a simplified NLG in an approach flight phase (the so-called *LAGooN* research program). The resulting noise source maps were then analyzed from the points of view of phenomenology (noise source mechanisms) and methodology (noise localization methods).

The present paper sums up the main steps and outcomes of such an investigation, being organized as follows: Sec. II briefly recalls the *LAGooN* experimental and numerical campaigns from which the noise source signals to be array-processed were excerpted. Then, Sec. III presents the methodology used for doing so, summarizing both the noise localization techniques employed and the practical ways the latter were applied to the present NLG configuration. Section IV then provides the noise source localization results obtained, discussing their phenomenological and methodological outcomes. Finally, Sec. V briefly summarizes the outcomes of the present study, as well as the current perspectives for extending it to other realistic problems coming from the aerospace industry.

II. Background: Experimental and Numerical Characterization of the Aeroacoustics of a Nose Landing Gear

The present study took direct benefit from the *LAGooN* project, which was supported by Airbus and conducted by several partners (ONERA, DLR, Southampton University, etc.). The primary objective of the project was to acquire an experimental database

Presented as Paper 2016-2844 at the 22th AIAA/CEAS Aeroacoustics Conference, Lyon, France, 30 May–1 June 2016; received 20 September 2016; revision received 25 April 2017; accepted for publication 11 July 2017; published online 24 August 2017. Copyright © 2017 by ONERA. Published by the American Institute of Aeronautics and Astronautics, Inc., with permission. All requests for copying and permission to reprint should be submitted to CCC at www.copyright.com; employ the ISSN 0001-1452 (print) or 1533-385X (online) to initiate your request. See also AIAA Rights and Permissions www.aiaa.org/randp.

*Senior Research Scientist, Department of Aerodynamics, Aeroelasticity and Acoustics. Member AIAA.

†Senior Research Fellow, Department of Aerodynamics, Aeroelasticity and Acoustics; stephane.redonnet@onera.fr (Corresponding Author). Member AIAA.



Fig. 1 A380 aircraft with landing gears deployed. Source: Emirates Airline and Manchester airport.

associated with elementary landing gear configurations so that computational methods dedicated to landing gear noise prediction can be accurately and thoroughly validated.

A. Experimental Characterization of the Aeroacoustics of a Nose Landing Gear

Within the LAGooN framework, combined experimental campaigns were carried out, focusing on both the aerodynamics and the acoustics of a simplified landing gear configuration [5,6]. The model geometry was that of an NLG of an Airbus A320 aircraft, with a scale factor of 1:2.5 applied and with only the main elements (leg, strut, wheels) kept (see left side of Fig. 2). The model was considered as isolated, that is, free of any airframe components (e.g., fuselage). It was tested for a wide range of flight conditions, whether it is in terms of flow speed (8 Mach numbers, M , from 0.1 to 0.28) or direction (11 yaw angles, β , from -12.5° to $+12.5^\circ$).

Conducted in ONERA's aerodynamic facility named "F2," the aerodynamic measurements first focused on the wall pressure field, which was explored through an extensive set of steady and unsteady pressure probes located on the NLG surface (wheels, strut, and axle). In addition, for two specific configurations (corresponding, respectively, to typical take-off and approach flight phases: $M = 0.23$ or 0.18 , $\beta = 0^\circ$), the steady/unsteady velocity fields occurring around the NLG model were accurately characterized using 2D particle image velocimetry (PIV) as well as 2D/3D laser Doppler velocimetry (LDV). Additionally, for these two configurations, mixed measurements (hot-wire plus 2D LDV) were performed in the wake of the landing gear so that complementary information is provided (e.g., two-point correlations).

Second, the acoustic measurements were achieved within ONERA's anechoic facility named CEPRA19 (hereafter referred to as C19) after it

was checked that the associated NLG aerodynamic near field was similar to that recorded within F2 installation, which was done by means of specific measurements and dedicated simulations [steady computational fluid dynamics (CFD) calculations]. These acoustic measurements first focused on the LG noise radiation, whose directivity was recorded in the far field at a distance of approximately $40R_w$ from the model, with R_w standing for the NLG wheel radius. Measurements were performed thanks to 12 microphones equally distributed over two arcs located in fly-over and sideline directions, respectively.

Finally, for more specific noise source identification purposes, dedicated measurements were performed in both F2 and C19 facilities to record the acoustic signals over microphone arrays of various designs and locations (i.e., a star-shaped array of 120 microphones and a cross-shaped array of 41 microphones that were respectively located $5.2R_w$ and $13R_w$ away from the gear in either the sideline or the fly-over direction).

The 14th and 15th AIAA-CEAS Aeroacoustics Conference provided an opportunity to thoroughly detail these two experimental campaigns and subsequent results [5,6]. In addition, recently, part of the associated experimental database was disseminated internationally through the so-called Benchmark for Airframe Noise Computations (BANC) workshop [30], allowing numerous research teams to validate their numerical capabilities with respect to the prediction of landing gear aeroacoustics [31].

B. Numerical Characterization of the Aeroacoustics of the Nose Landing Gear

In that regard, for instance, several simulations of the NGL configuration were conducted at ONERA, all performed following a *hybrid* strategy—for which the noise generation and propagation stages are split and solved successively, as opposed to the *direct* approach, where both are simulated simultaneously.

As the first step of the hybrid scenario, the noise generation stage was simulated through 3D unsteady compressible CFD calculations [17,32], which relied on the so-called zonal detached eddy simulation (ZDES) approach, for which ONERA's *elsA* solver [31] was used.

As an illustration, Fig. 3 depicts the results obtained for that particular configuration corresponding to a typical approach flight phase ($M = 0.18$, $\beta = 0^\circ$), which will be solely considered throughout the present paper. As shown in the right side of this figure, the CFD calculations were favorably compared with the aerodynamic measurements through direct comparison of near-field results (with the exception of mismatches over the low- and high-frequency ranges, the latter of which can be reasonably attributed to the high-pass filtering induced by the numerical simulation). In particular, as experimental outputs, numerical ones exhibited tonal features whose frequency f was approximately 1 and 1.5 kHz. Radiating primarily in the sideline directions, these tonal features were inferred to be induced by resonances coming from the wheels' inner cavities.

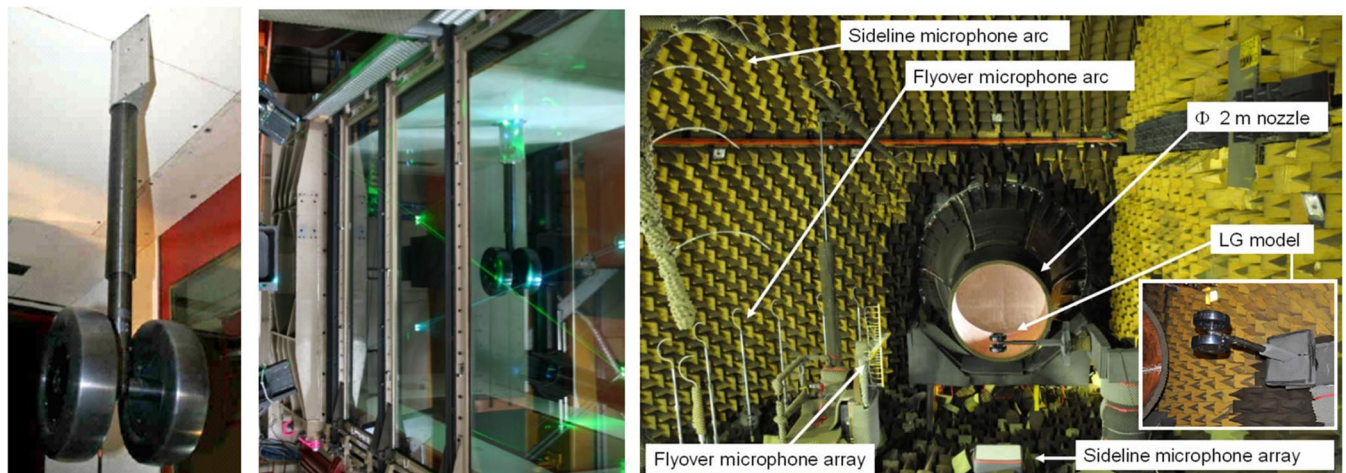


Fig. 2 Experimental characterization of the NLG noise emission/radiation via aeroacoustics tests. NLG model (left) installed in ONERA's F2 aerodynamic facility (center) and C19 anechoic wind tunnel (right).

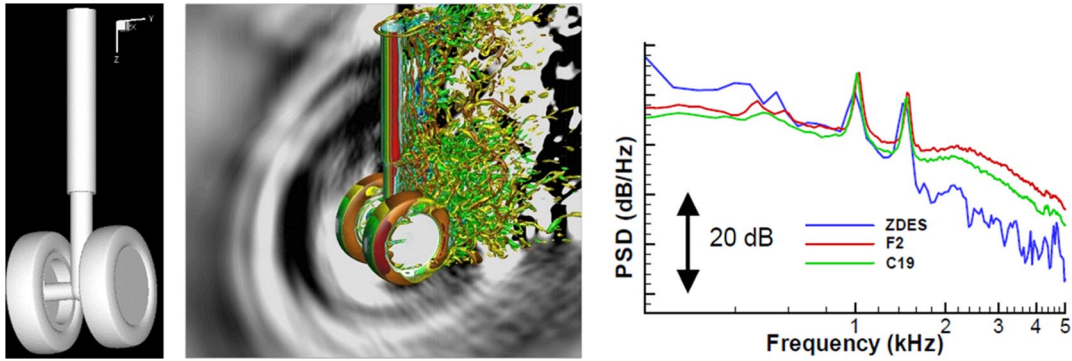


Fig. 3 Numerical characterization of the NLG noise emission via unsteady CFD calculations. Left: NLG model. Center: near-field CFD outputs (Q-criterion isosurfaces and instantaneous pressure fluctuation field). Right: validation via direct comparison of the power spectral density delivered by CFD (blue) and experiments (red and green) for a probe located on the right wheel. CFD calculation by Dr. S. Ben Khelil (ONERA, elsA solver).

As for what has been done regarding the experimental database, part of the CFD dataset was disseminated through the BANC workshop (as category 8), allowing various research centers (e.g., NASA, JAXA, ONERA) and universities (e.g., Old Dominion University, Campinas University) to benchmark the computational techniques employed for the acoustic propagation stage [33]. In that regard, use was here made of an advanced hybrid approach [34,35] whose noise propagation stage relied on computational aeroacoustics (CAA) rather than on an integral method (IM) such as the Acoustic Analogy by Ffowcs-Williams & Hawkings (FWH), such as usually done. This aimed at ensuring a higher fidelity in the acoustic propagation stage by 1) accounting for the noise emission that was effectively predicted by the CFD stage (rather than modeling it via equivalent sources, as implicitly done by IM/FWH techniques) and 2) possibly considering the realistic jet flow characterizing the experiment (rather than modeling it via a simplistic uniform mean flow, as also done by IM/FWH techniques). After that, the CFD-based noise generation stage previously simulated was weakly coupled with a CAA-based noise propagation one, the latter conducted using ONERA's *sAbrinA* solver [34–36], which is a time-domain CAA code that solves the perturbed nonlinear Euler equations using high-order finite-differences schemes. The 19th and 21st AIAA Aeroacoustic Conference provided an opportunity to present these CFD-CAA hybrid calculations and outcomes [33,37], which were then thoroughly documented in a dedicated journal paper [32] and are briefly summarized hereafter.

The first CFD-CAA hybrid calculation corresponded to the isolated NLG; that is, it incorporated a uniform mean flow corresponding to a homogeneous and unbounded medium. This calculation allowed validation of the methodology employed through direct comparison of

the CFD-CAA results against the C19 experimental records (which were corrected from the open jet flow effect), as well as against the numerical outputs coming from more traditional AA-extrapolations (by NASA, JAXA, and ONERA) [33]. For the second CFD-CAA hybrid calculation, the NLG was considered as installed within the C19 anechoic wind tunnel, that is, with a heterogeneous mean flow matching the realistic steady jet occurring in the facility. This alternative calculation made it possible to enhance further the fidelity of the prediction by CAA, accounting for the facility jet flow effects that had possibly weighted the experimental measurements. As an illustration of these two hybrid calculations, Fig. 4 first depicts a snapshot of the instantaneous perturbed pressure field obtained at the end of the CFD-CAA computation associated with the C19-installed NLG configuration (see Fig. 4, left-side image). As indicated, once forced within the CAA domain through the CFD-CAA interface (small cubic box, drawn here in purple), the CFD source signal is CAA-propagated up to the far field.

Regarding the isolated NLG configuration (i.e., associated with a uniform flow), the center side of Fig. 4 provides the spectrum of the CFD-CAA signal recorded for a probe located in the midfield flyover direction (approximately $13R_w$ away from the model), comparing it against that of its experimental counterpart. This validation exercise is quite satisfactory if one considers the good match of spectra delivered by both the experimental measurements (in black) and the CFD-CAA-coupled calculation (in red), despite their very disparate signal durations (20 s vs 0.05 s). For indicative purposes, the same image also provides the spectra from more traditional CFD-IM hybrid calculations by NASA and JAXA (depicted in blue and green, respectively), which were obtained for the same isolated NLG configuration using the so-called porous-surface FWH integration technique.

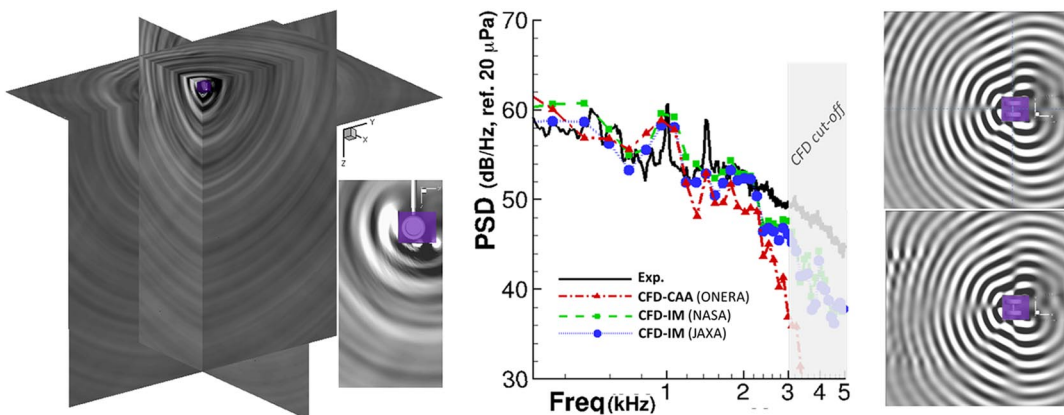


Fig. 4 Numerical characterization of the NLG noise emission/radiation via CFD-CAA hybrid computations. Left: Near- to far-field noise radiation (instantaneous perturbed pressure) by the C19-installed NLG as delivered by the second CFD-CAA computation (realistic jet flow). Center: Midfield noise radiation (power spectral density) by the isolated NLG, as delivered by the first CFD-CAA computation (uniform flow, in red) and compared with either experimental (black) or alternative CFD-IM computational (blue and green) outputs. Right: refraction effects of C19 jet flow onto the NLG tonal noise emission ($f = 1.5$ kHz) highlighted through the instantaneous perturbed pressure field delivered within the xy plane by either the isolated NLG (top) or the C19-installed NLG (bottom) calculations. CFD-CAA interface appears as a small purple box.

Finally, the effects of the C19 facility's heterogeneous jet flow onto the NLG acoustic emission are highlighted in the right side of Fig. 4, which compares the instantaneous perturbed pressure field associated with the second tonal emission ($f = 1.5$ kHz), as delivered within the xy plane at the end of the CFD-CAA calculation associated with either the isolated or the C19-installed NLG configuration (top and bottom images, respectively). As indicated, when the realistic jet flow is accounted for, the acoustic waves see their patterns modified as they cross the jet shear layers and then propagate within a region where the medium is at rest. Compared with what happens when the medium is homogeneous, these refraction effects affect the acoustic signature in a nonnegligible manner, leading to differences in terms of directivity, as well as in terms of radiated power. Here, it is worth mentioning that a standard CFD-IM hybrid approach could not be used to perform such an assessment of the installation effects of the facility environment because of the underlying hypothesis (e.g., homogeneous propagation medium) the IM stage relies on.

For more details about these CFD-CAA weakly coupled calculations and their underlying hybrid methodology, the reader is referred to [32,37].

III. General Methodology and Practical Implementation

Once the aeroacoustics by the NLG had been experimentally and numerically characterized, its underlying noise mechanisms were investigated further by means of source localization techniques. This was achieved through an application of CBF and DAMAS [38] sensor array methods to the time series that had been recorded on purpose over dedicated microphone arrays, both in the experiments and in the CFD-CAA computations. The present section summarizes the methodology employed for doing so.

A. Acquisition of the CFD-CAA Signals

As mentioned previously, the first CFD-CAA simulation was allotted a uniform mean flow to ease both 1) the cross-validation of the CAA-based hybrid method against more traditional IM-based ones [33] and 2) the assessment of the refraction effects possibly induced by the facility jet flow, which was then incorporated into the second CFD-CAA simulation.

Because of its uniform mean flow, with the confinement effects excepted, the first CFD-CAA simulation was similar to the aerodynamic experiment that was run in the F2 aerodynamic/closed

test section wind tunnel, which incorporated the star-shaped localization array composed of 120 microphones located $5.2R_w$ away from the gear. In contrast, thanks to its C19-based background mean flow, the second CFD-CAA simulation was similar to the acoustics experiment conducted in the open jet anechoic facility, which incorporated the cross-shaped localization array composed of 41 microphones located $13R_w$ (i.e., $2R_j$) away from the gear (R_j indicating the jet radius at the C19 nozzle exit).

For simplicity's sake, both CFD-CAA computations were prescribed an identical storage of the numerical signals, which were thus acquired over a total of 161 microphones (corresponding to both arrays; see Fig. 5). Please note that each storage location was approximated by the closest grid point of the Cartesian mesh used for running the CAA stage, for the stored signals do not have to be space interpolated (and thus possibly degraded). It was, however, checked that the location errors to be possibly induced by such an approximation were negligible, given the high density of the CAA grid over the midfield areas where the storage was to occur. In the same way, the CFD-CAA signals were not interpolated or sampled in time, being acquired for the entire simulation (transient included)—all this leading to a time series of 14,000 steps acquired with a regular time step of $5 \mu\text{s}$ (i.e., 0.07 s of physical time). All the above must be compared against the acquisition characteristics used in the experiments, following which F2 (resp. C19) array signals were recorded at the exact microphone locations for a total of 1,966,080 (resp. 864,256) steps acquired with a time step of $5 \mu\text{s}$ (resp. $25 \mu\text{s}$), that is, approximately 9.8 (resp. 21) seconds of physical time.

Given their disparate acquisition characteristics ($1,966,080 \times 5 \mu\text{s}$ vs. $864,256 \times 25 \mu\text{s}$ for F2 and C19, respectively), the experimental signals were time-averaged differently, as the resulting frequency bandwidth Δf is the same ($\Delta f = 250$ or 500 Hz). These frequency bandwidths were also targeted for the numerical signals, whose much shorter duration ($14,000 \times 5 \mu\text{s}$) imposed that the number of averages is drastically reduced. Please note that only the outcomes associated with the higher-frequency bandwidth (500 Hz) are provided below. In addition, both the experimental and numerical signals were FT-processed with a Hanning window applied (no overlap).

B. Exploitation of the CFD-CAA Signals Through Sensor Array Methods

The resulting spectral signals were then array-processed through CBF and DAMAS localization methods, which were implemented within a single in-house ONERA code. The latter code was optimized on purpose, through both an increase in its algorithmic efficiency (to

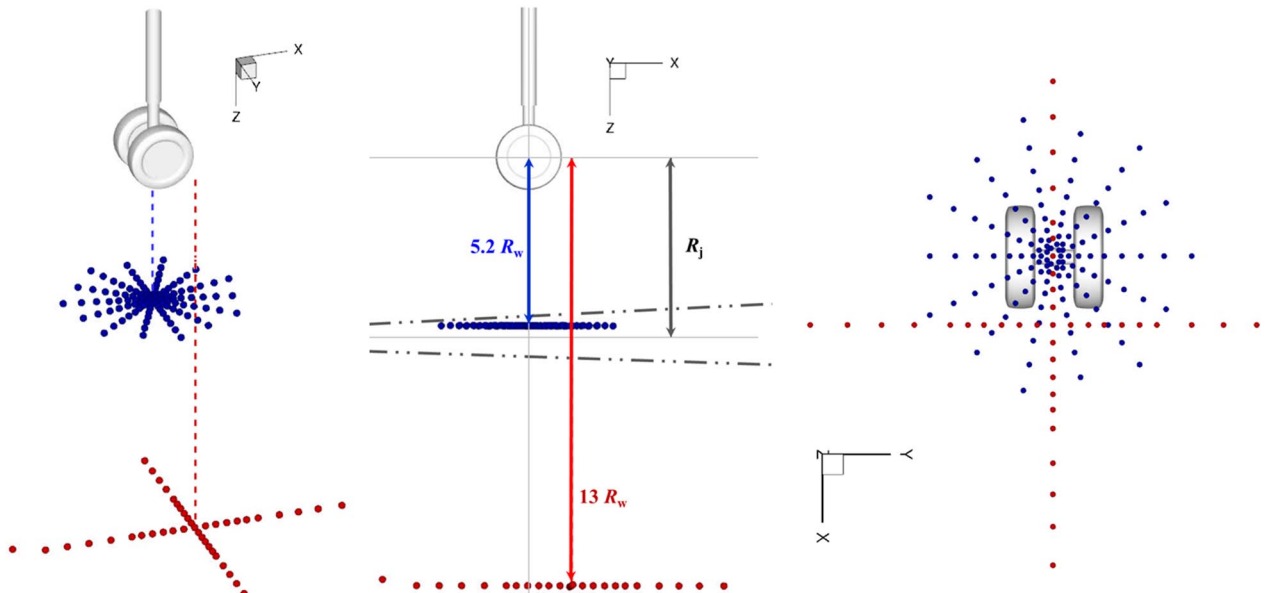


Fig. 5 Virtual microphone arrays for the acquisition of CFD-CAA signals. F2-based star-shaped (in blue) and C19-based cross-shaped (in red) microphone arrays. R_w indicates the NLG wheel radius, whereas R_j stands for the open jet radius at the nozzle exit (C19-based configuration only).

speed up the DAMAS convergence) and the incorporation of an advanced propagation kernel. Indeed, noise localization methods include a propagation model whose role is to artificially retropropagate the recorded acoustic signals up to the (arbitrarily chosen) focalization area to locate the noise sources sought. Such a propagation kernel is generally based on simple models (homogeneous free-field, parallel shear layers, etc.), in which numerical solving relies on analytical formulas (Green functions, Amiet's models, etc.). However, an indirect objective of the present study was to assess the ability of noise localization methods to account for the refraction effects of realistic background flows when equipped properly (e.g., the round spreading-out jet of the C19 anechoic wind tunnel). Therefore, in the present case, the propagation kernel was allotted a geometrical acoustics (GA) approach based on works by Candel [39,40]; implying solely a high-frequency approximation (i.e., assuming an acoustic wavelength that is small enough compared with the length scale of flow heterogeneities), this approach accurately accounts for the refraction effects of any type of mean flow, as was recently confirmed through a dedicated numerical study [41] by the present authors. Please note that, in the present case, the GA-based propagation kernel was each time adjusted to the configuration considered; whenever the latter configuration involved a homogeneous medium (e.g., the F2 experiment, first CFD-CAA computation), the latter kernel was reduced to the convected Helmholtz equation (Green function). In contrast, when the configuration involved the realistic jet (e.g., the C19 experiment, second CFD-CAA calculation), the propagation kernel accounted for the heterogeneous mean flow used within the CAA stage.

The CBF method was run as is, given its relative simplicity and robustness. In contrast, given its higher complexity and sensitivity, the DAMAS method was tuned with care through dedicated parametric studies. Indeed, as mentioned earlier, although more accurate than CBF, DAMAS comes with greater sensitivity to various factors, such as the way of 1) evaluating the cross-spectral densities from the recorded acoustic signals (e.g., parametric or nonparametric methods) and/or 2) array-processing them effectively to produce noise source maps (e.g., focalization area, algorithm convergence, regularization parameters). Assessing the sensitivity of DAMAS was here achieved by varying its parametrization; first, the noise source focalization area was allotted various dimensions. Then, the DAMAS localization algorithm was run with several levels of convergence considered. Finally, a regularization process (based on the classical approach by Tikhonov [42]) was applied to all localization results, the regularization rate being varied. Please note that, given the important number of localization exercises and outputs such parametric study led to, only the most meaningful outcomes are discussed in Sec. IV. They correspond to the following conditions: the noise source focalization area is of medium size, that is, a

$60 \times 60 \text{ cm}^2$ xy section centered on the landing gear strut and meshed with 31×31 grid points regularly spaced (see the left side of Fig. 6). The convergence level corresponds to the lower one applied, such that 10 s was sufficient to reach a steady state in terms of residuals. Finally, the regularization rate that was jointly applied to both the numerical and experimental results is associated with a value that was solely adjusted to the configuration considered (F2 or C19), given the important differences between both cases (arrays, facilities, etc.).

Regarding the visualization of all CBF and DAMAS localization results, an identical dynamic of 10 dB was chosen, its min/max bounds adjusted to the strength of the source level observed for each case (F2 or C19 configuration, experimental or numerical signals, localization method, targeted frequency, etc.). As an illustration, the right side of Fig. 6 depicts the NLG noise sources associated with the 1.0 kHz tonal emission, as derived via an application of DAMAS to the numerical signals extracted from the first (i.e., as-like F2) CFD-CAA simulation, whose near-field aerodynamics and midfield acoustics results appear here in black lines and colored floods, respectively.

IV. Results and Discussion

As stated above, various cases were addressed depending on whether the considered configuration was similar to that of the F2 or C19 experiments. For each case, two localization exercises were performed using either CBF or DAMAS approaches.

A. Localization Results Associated with the F2-Based Configuration

First, localization exercises focused on the star-shaped array located $5.2R_w$ away from the gear used in the F2 experiments. Compared with the alternative one (the C19 experiment and associated calculations), this particular configuration offered the advantages of being characterized by 1) a better resolution of the array (given its higher aperture angle, that is, array radius vs. distance to focalization area), and 2) the absence of refraction effects (given the roughly homogeneous flow surrounding the gear). Regarding the F2 experimental signals, however, some biases were expected to come from the confined character of the vein (closed test section); first, the acoustic reverberation by the vein's walls could have contaminated the noise signals propagated up to the array with extra (indirect) noise. This effect was, however, expected to be partly removed *a posteriori* by the localization procedure. Second, the turbulent flow boundary layer along the walls could have induced additional biases onto the propagated noise signals because of hystacking effects (i.e., acoustic diffusion by turbulence). This bias was, however, expected to be modest, given the relatively low frequency of the noise emission.

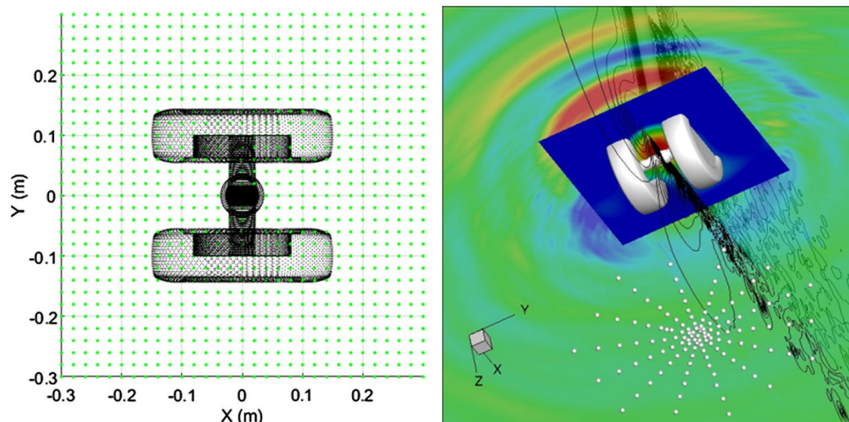


Fig. 6 NLG noise source localization through CBF and DAMAS sensor array methods. Left: Focalization grid used for CBF and DAMAS localization exercises. Right: NLG noise sources associated with the numerical signals extracted from the first (i.e., as-like F2) CFD-CAA computation, and exploited via DAMAS (star-shaped array appears as white dots); near-field aerodynamics (CFD solution in black lines), mid-field acoustics (CAA solution in flood, out of the blue square focalization area), and noise source at 1 kHz (DAMAS solution in flood, within the blue square focalization area).

1. Noise Source Maps by CBF and DAMAS

Figure 7 depicts the noise source maps derived from these F2 experimental signals, comparing the outputs delivered by the CBF and DAMAS approaches. As shown, for both cases, noise sources clearly emerge in the vicinity of the NLG area, allowing perception of some trends in their dynamics; according to CBF maps, the noise sources are mostly located within the wheel area, although they move slightly downstream of the gear when the frequency increases. Compared with the CBF maps, the DAMAS maps are still more explicit, revealing noise sources that are localized better—although sometimes slightly contaminated with spurious artifacts, especially for the higher frequencies (see what happens at the immediate periphery of the wheel area, for $f = 2$ and 2.5 kHz). This higher capacity of DAMAS for pinpointing noise sources indeed comes from its intrinsic modeling, which replaces the actual noise emission areas with punctual *equivalent* uncorrelated sources. Although one must be cautious when it comes to interpreting such equivalent results (especially if the noise sources are noncompact, as is the case here); however, they offer the opportunity to draw some meaningful trends about the noise emission mechanisms. For instance, here, DAMAS maps indicate noise sources that are either centered on the strut or located downstream of the gear. This corroborates the observations and interpretations previously made about the noise source

mechanisms by this particular NLG, which are likely to be composed of both cavity resonances (global mode localized within the wheel area) and fluid–structure interactions (impingement of the flow onto the landing gear strut and wheels).

This last observation is further confirmed by the numerical counterpart of the previous localization exercise, that is, the array exploitation of the CFD-CAA signals coming from the first computation (i.e., based on the uniform flow, given the roughly homogeneous character of the flow field surrounding the gear in the F2 experiment). Figure 8 depicts the resulting noise source maps, as obtained from both the CBF and DAMAS approaches.

As shown, the observations previously made for the experimental results are here recovered, and further completed (especially for the DAMAS maps). Indeed, one can here better appreciate how the two tonal noise sources (1 and 1.5 kHz) appear to be located right between the wheels, whereas their higher-frequency counterparts appear to be positioned downstream of the strut, in the wake or on the wheels themselves. As stated above, these observations can be viewed in light of a dedicated study [5,6] that was originally conducted via specific dimensional analyses (tonal frequency vs. wheel dimensions) and parametric studies (tonal frequency vs. flow speed) during the F2 experiments; the conclusions were that the tonal peak emissions (1 and 1.5 kHz) were related to acoustic resonances

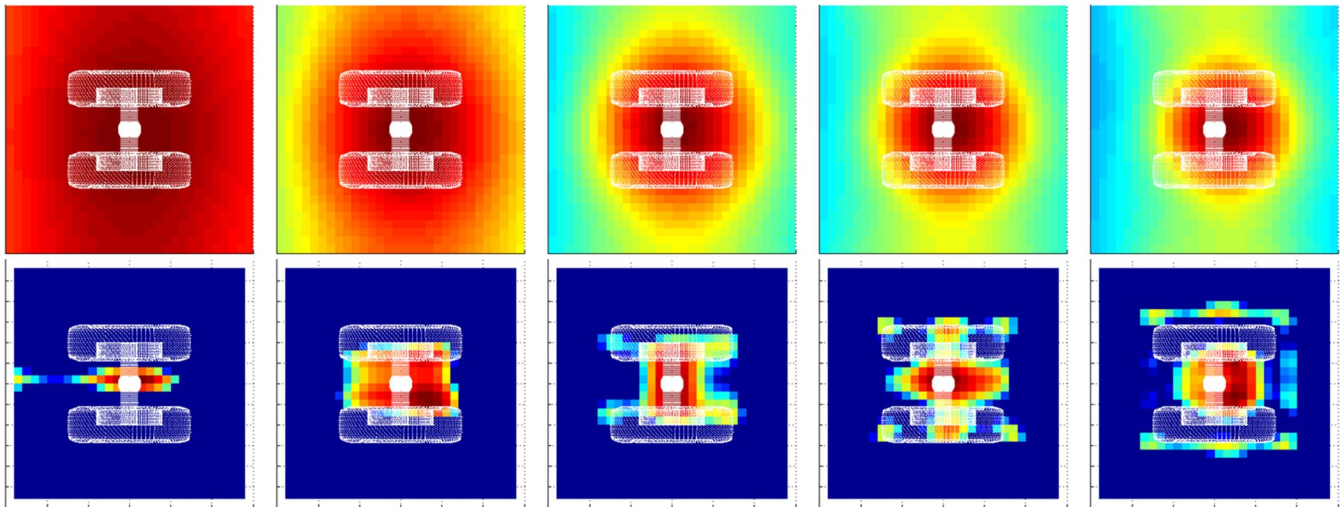


Fig. 7 NLG noise sources associated with the experimental signals extracted from F2 experiments (star-shaped array, closed test section, quasi-uniform flow), and exploited via either CBF (top) or DAMAS (bottom). Source maps obtained over an xy patch of 60×60 cm² for acoustic emissions at 1, 1.5, 2, 2.5, and 3 kHz (from left to right).

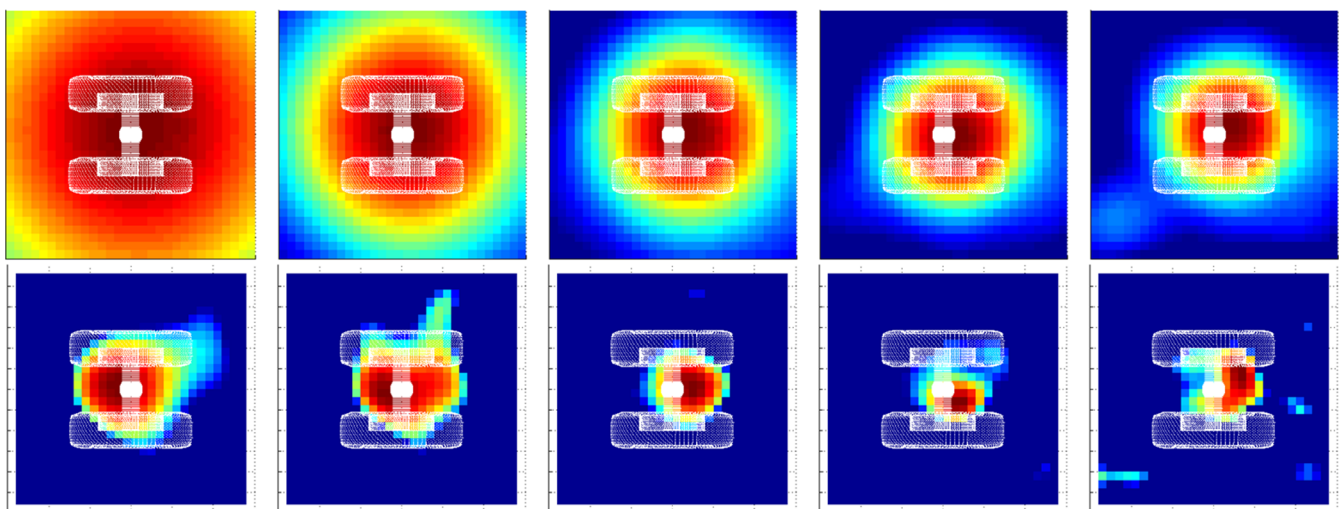


Fig. 8 NLG noise sources associated with the numerical signals extracted from the first (i.e., as-like F2) CFD-CAA computation (star-shaped array, free-field, uniform flow) and exploited via either CBF (top) or DAMAS (bottom). Source maps obtained over an xy patch of 60×60 cm² for acoustic emissions at 1, 1.5, 2, 2.5, and 3 kHz (from left to right).

occurring within the wheel cavity, whereas the other (broadband) emissions were associated with the fluid–structure interactions of the turbulent flow impinging the landing gear structure.

Here, it is worth noting that, except for the slight differences inherited from the spurious artifacts coming from the testing conditions (e.g., confinement effects), the noise maps derived from the numerical signals (see Fig. 8) are very similar to those originating from their experimental counterpart (see Fig. 7).

2. Integrated Power Spectral Density of DAMAS Noise Source Maps

Given the high variability of DAMAS method upon the nature of acoustic signals it is fed with, it is not rare that a localization exercise provides rather disparate results, depending on the way such exercise is conducted (e.g., frequency analysis bandwidth, focalization area, algorithm convergence, regularization parameters) and exploited (e.g., plotting dynamics). This, in particular, may not only render more difficult the proper physical interpretation of localization outputs but also question their tentative validation through cross comparisons (e.g., between the noise source maps derived from either the experimental or the numerical signals, here). In practice, one can thus check and/or compare various localization results by converting the associated noise source maps into a single power spectral density (PSD) spectrum, that is, by integrating its noise source intensity levels over the focalization area. This is what was achieved for the present DAMAS results and is depicted in Fig. 9, which displays (in red) the integrated spectrum obtained for each of the DAMAS noise source maps provided in Figs. 7 and 8. These integrated PSD spectra are compared with those recorded at a single microphone (central position), which are here depicted in black. Finally, the same figure also displays (in blue) alternative integrated PSD spectra corresponding to an integration performed over a smaller region of the noise source focalization area (see the thumbnail picture in the left side of Fig 9). The reason for arbitrarily restricting the PSD integration to this immediate vicinity of the gear is to de-bias it from possible spurious extra noise sources, which are generally spread out around the actual noise source area.

As shown in the right side of Fig. 9, both the experimental and the numerical outputs deliver PSD spectra that are very similar from a qualitative point of view; in particular, it is clear that all spectra similarly decay when the frequency increases, which is coherent with the NLG noise signature itself (see the near- and mid-field noise spectra in Figs. 3 and 4, respectively).

In contrast, whereas F2 numerical signals deliver results that collapse almost perfectly (see the right side of Fig. 9), their experimental counterparts lead to spectra that are scattered and characterized by higher values. This effect is due to the inherent

background noise of the F2 aerodynamic facility, which was here exacerbated by the confined and reverberant nature of its closed test section. Indeed, here, not only was the facility background noise added to the NLG noise itself but also both components were then reflected by the test section walls in multiple ways. As a logical result, the localization exercise was partly biased because of the resulting amplitude and phase interferences, which may vary depending on the frequency and the microphone location. This being said, because these interferences do not fit the source model, the DAMAS method appears to have been able to filter out a significant part of such background and reverberated noises (between 6 and 10 dB, depending on the frequency). This can be inferred from the mismatch between the single-array (central) microphone and the baseline (global) integrated PSD spectra (in black and red, respectively). However, such intrinsic filtering by DAMAS visibly did not prevent some spurious noise sources from being artificially created all over the focalization area because of the noisy and reverberant environment. This can be first inferred from the 2 to 6 dB mismatch between the baseline (global) and the alternative (local) integration results (see the red and blue lines on the left side of Fig. 9), which indicates that some spurious noise sources were abusively localized at the periphery of the NLG closer area; although of lower amplitude than the floor threshold of the DAMAS noise source maps (see the bottom images of Fig. 8), once cumulated, these fake sources enhanced the global integrated PSD spectrum. In addition, one can suspect the NLG closer area also to have been polluted by fake sources when comparing the previous alternative (local) integrated PSD spectrum against that of its numerical counterpart (see the blue curves in the left and right side of Fig. 9, respectively); when submitted to the arbitrary removal of 7 dB over the entire frequency range, the locally integrated PSD associated with the F2 experimental results collapse almost perfectly with that coming from the numerical ones (see cyan curve in Fig. 10).

In this stage, it is remarkable how remarkably consistent these PSD spectra of the numerical outputs are; indeed, for all frequencies, the levels associated with the single microphone, the local and the global integration, are very close, their differences falling within a 2–3 dB range. Although this obviously benefited from the fact that, here, the localization exercises were not corrupted by the installation effects weighing on the experiments, this proves that most of the NLG sources are located in the immediate vicinity of the gear (local integration area). Then, from a more methodological point of view, this confirms the validity of the DAMAS method implementation and underlying components (e.g., source model). Finally, this further demonstrates that, despite—and sometimes because of—their intrinsic differences with experiments (e.g., shorter but less corrupted noise signals), unsteady CFD-based calculations can be exploited as

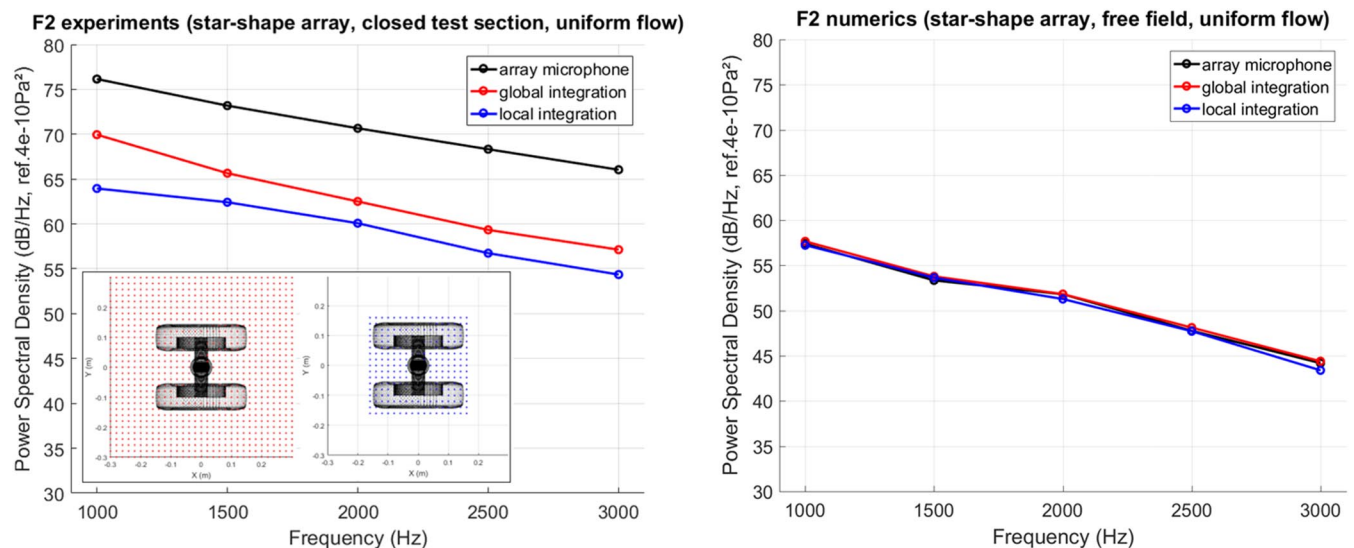


Fig. 9 Integrated PSD spectrum of the NLG noise source maps obtained through a DAMAS exploitation of either the experimental (left) or the numerical (right) signals associated with the F2-based configuration.

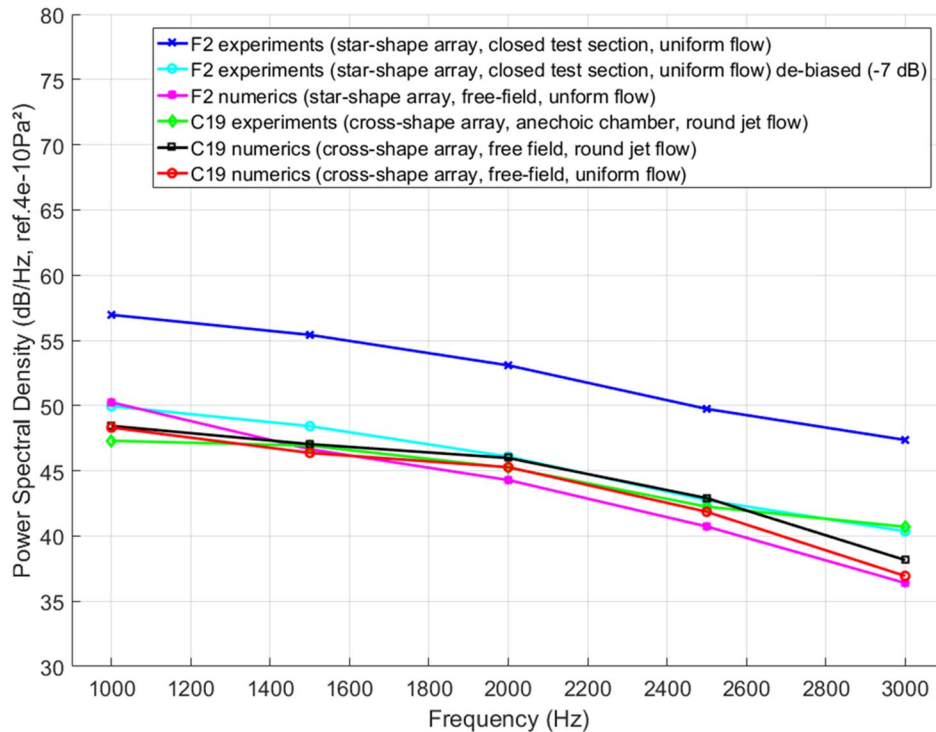


Fig. 10 NLG noise sources associated with all signals, once integrated over a restricted area (red dots in the top/left image) and plotted as PSD spectra (right image): F2 experiment in blue, F2 experiment de-biased from the background noise in cyan, as-like F2 computation in pink, C19 experiment in green, and as-like C19 computations (round jet and uniform flow) in black and red, respectively.

efficiently as experimental tests through array localization methods. This observation confirms the conclusions recently drawn by various authors [43,44], speaking in favor of a more systematic use of noise localization methods within a computational context.

B. Localization Results Associated with the C19-Based Configuration

Second, localization exercises focused on the cross-shaped array located $13R_w$ (i.e., $2R_j$) away from the gear used in the C19 experiments. Compared with the previous one (the F2 experiment and associated calculations), this particular configuration had the disadvantages of being characterized by 1) a lower resolution of the sensor array (given its lower aperture angle) and 2) the existence of refraction effects (given the presence of the open jet flow). In contrast, still compared with the previous F2-based configuration, the experimental signals were now expected to be free of any contamination coming from reverberation, given the anechoic character of the C19 facility.

1. Noise Source Maps by CBF and DAMAS

Figure 11 displays the noise source maps obtained from these C19 experimental signals, comparing the outputs delivered by both the CBF and DAMAS approaches.

As shown, the results are very similar to those previously derived from the F2 experiment (see Fig. 7), a few differences excepted. In particular, compared with the previous case, the CBF maps now exhibit a cross-shaped halo. The latter simply comes from the point spread function (PSF) inherited from the particular design of the cross-shaped array, which contaminates the CBF localization results. In contrast, such an effect is absent from the maps delivered by DAMAS, whose intrinsic formalism allows easier suppression of these types of spurious artifacts (through the proper taking into account of the array's PSF). Apart from that, the DAMAS results also appear to be free from the spurious background noise and reverberation effects that had slightly contaminated the previous F2-based outputs over the higher frequencies because of the confined character of the vein (see Fig. 7, bottom-right images). At the end, the present C19-based DAMAS noise maps (Fig. 11, bottom images) are both very similar to their previous F2-based counterparts (Fig. 7,

bottom images) and much clearer than their C19-based CBF equivalents (Fig. 11, top images), thus revealing still better the physical noise sources occurring around the NLG—and all over the spectrum.

The numerical counterpart of the previous C19-based experiment noise maps (Fig. 11) is provided in Fig. 12, which depicts the CBF and DAMAS outputs derived from the numerical signals delivered by the second CFD-CAA computation (i.e., based on the round jet flow characterizing the C19 installation). Here, one can see that the CBF maps still exhibit the cross-shaped halo, which is, however, deformed at higher frequencies ($f \geq 2.5$ kHz) because of a visible shift in the noise source area downstream of the gear. Again, the DAMAS outputs allow better clarification, thanks to their more accurate maps; indeed, one can see how, above 2.5 kHz, the noise sources that were initially located within the wheel area are now combined with additional noise sources, which appear to be positioned farther away downstream of the gear, in the wake region. Whereas the centered noise sources are similar to the (physical) ones seen previously, the extra noise sources are likely to find their origin in some spurious artifacts, which may have contaminated the numerical signals, thus corrupting part of the localization outputs.

At this stage, it is worth mentioning that, within the framework of an AIAA-supported workshop dedicated to sensor array techniques, the results depicted in Figs. 11 and 12 were cross-compared with those obtained by researchers from NASA Langley Research Center, who similarly applied CBF and DAMAS techniques to the present C19-based experimental and numerical datasets. For each of the configurations addressed (e.g., experimental or numerical signals) and/or noise localization method employed (e.g., CBF or DAMAS), noise source maps obtained from both sides were very close, exhibiting similar patterns. Regarding in particular the cross-shaped array localization results derived from the CFD-CAA dataset, the NASA maps were corrupted by the same type of spurious noise as the present ones, although such corruption occurred to a lesser extent apparently because of a different postprocessing method used). In addition to cross-validating the noise localization techniques used from both sides, such similarity between ONERA and NASA results indirectly confirmed that these spurious noise sources primarily

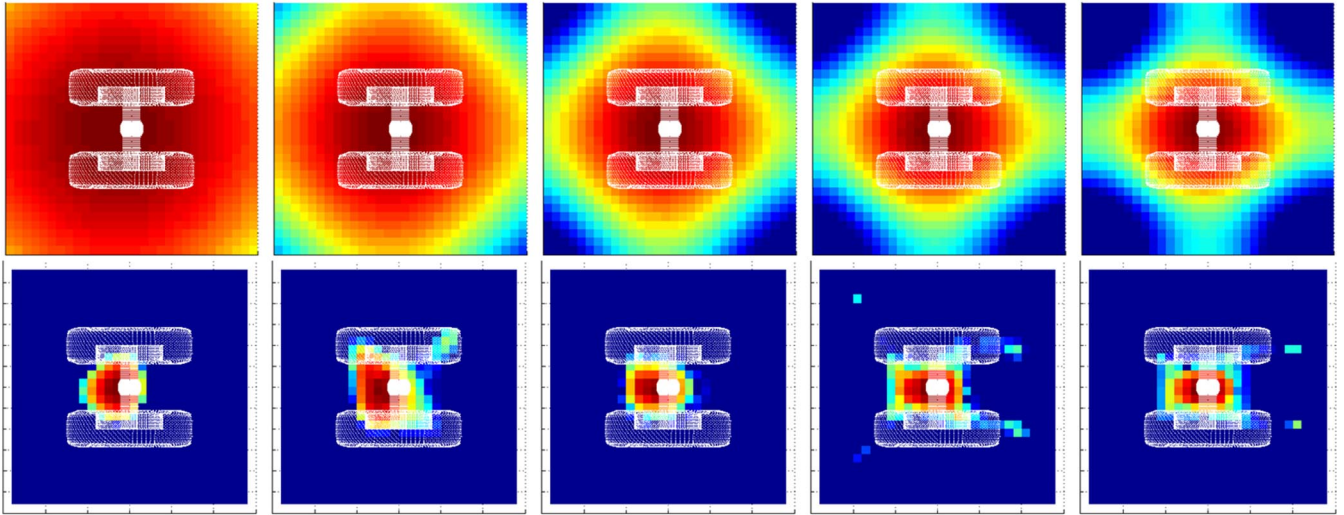


Fig. 11 NLG noise sources associated with the experimental signals extracted from C19 experiments (cross-shaped array, anechoic chamber, round jet flow) and exploited via either CBF (top) or DAMAS (bottom). Source maps obtained over an xy patch of 60×60 cm² for acoustic emissions at 1, 1.5, 2, 2.5, and 3 kHz (from left to right).

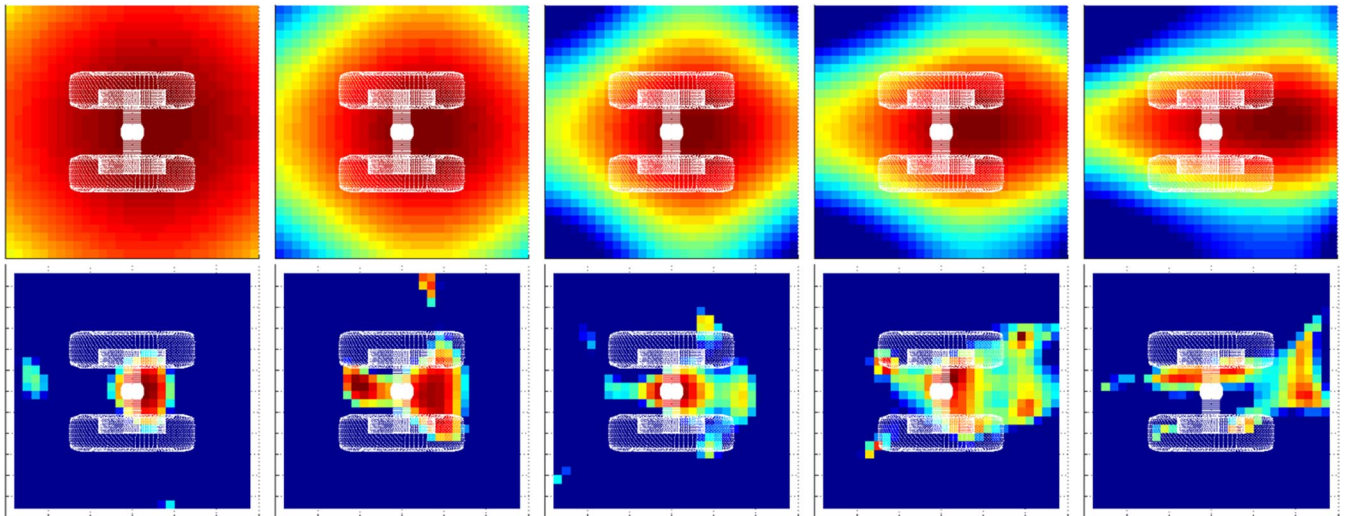


Fig. 12 NLG noise sources associated with the numerical signals extracted from the second (i.e., as-like C19) CFD-CAA computation (cross-shaped array, free-field, round jet flow) and exploited via either CBF (top) or DAMAS (bottom). Source maps obtained over an xy patch of 60×60 cm² for acoustic emissions at 1, 1.5, 2, 2.5, and 3 kHz (from left to right).

found their origin in the CFD-CAA numerical signals themselves, rather in the noise localization method employed.

At this stage, one might wonder whether these spurious artifacts could have something to see with refraction effects of the open jet, whose numerical treatment could have gone wrong, during either the CAA propagation stage or the localization retropropagation step. To this end, Fig. 13 displays the exact same cross-shaped array outputs as those of Fig. 12, except that they were now derived from the numerical signals delivered by the first CFD-CAA computation (i.e., based on a uniform flow), for which no refraction effects were involved at all. As one can see, the resulting noise source maps are very similar to those previously obtained under a realistic jet flow condition (see Fig. 12), which discards the hypothesis of spurious artifacts coming from incorrect numerical handling of refraction effects. Beyond that, such similarity between Figs. 12 and 13 outputs indirectly confirms that the refraction effects inherited from the facility jet were initially correctly taken into account by both the CAA and the noise localization stages. Indeed, if the latter had been incorrectly handled at some point, a shift in the noise source locations would have been noticeable between the two results.

Alternatively, this close similarity between the two outputs tends to prove that sensor array methods may be efficiently applied to

numerical simulations whose propagation stage is of lower fidelity, provided that its retropropagation stage is in line with the assumptions made (here, a uniform flow hypothesis). This encourages the exploitation by noise localization methods of more traditional hybrid numerical methods (e.g., CFD-IM hybrid calculations), for which the propagation stage generally relies on a simplistic propagation kernel (e.g., convected Green function). At this stage, however, one should keep in mind that, here, refraction effects were rather modest ($M = 0.18$); the present conclusions shall thus not be readily extended to other types of configurations, especially those for which flow conditions are severe. From a more global perspective, the above successful application of sensor array methods to this alternative CFD-CAA calculation speaks in favor of a more systematic use of noise source localization techniques within a computational context, given that numerical simulations may allow the virtual addressing of configurations that one could hardly handle in practice via experimentation. For instance, the alternative CFD-CAA simulation exploited here corresponds to a hybrid configuration between the F2 and C19 tests, thus reproducing virtually an in-flight experiment (i.e., uniform infinite flow within an unbounded space).

Regarding these spurious artifacts observed at higher frequencies for the cross-shaped array results derived from the second

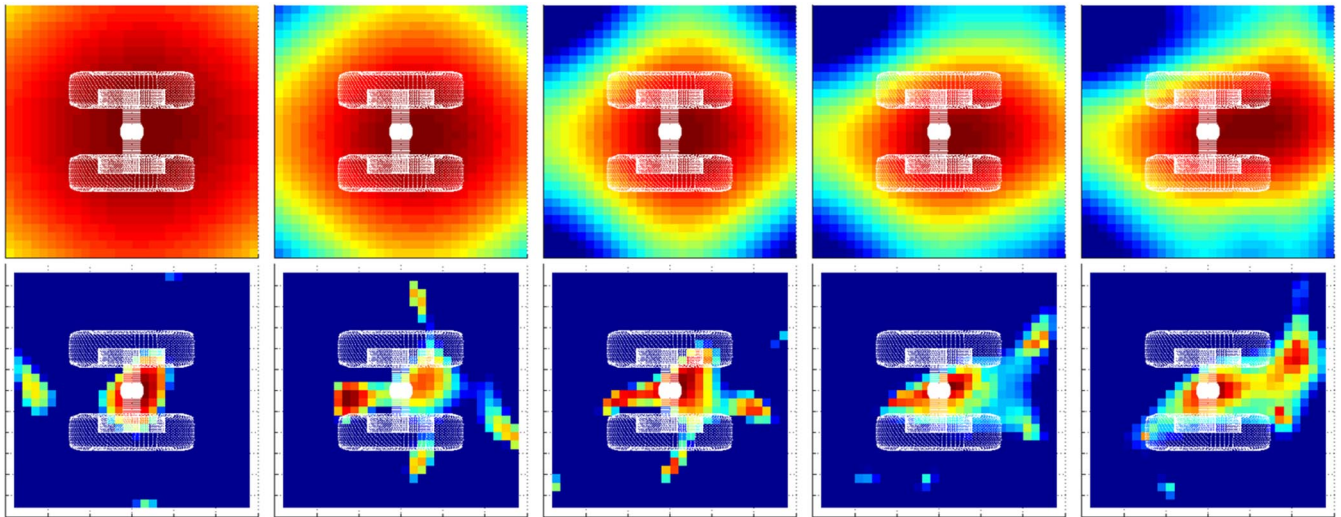


Fig. 13 NLG noise sources associated with the numerical signals extracted from the first (i.e., as-like F2) CFD-CAA computation (cross-shaped array, free-field, uniform flow) and exploited via either CBF (top) or DAMAS (bottom). Source maps obtained over an xy patch of $60 \times 60 \text{ cm}^2$ for acoustic emissions at 1, 1.5, 2, 2.5, and 3 kHz (from left to right).

CFD-CAA computation, a plausible explanation for this could come from the fact that, as was extensively documented in [37], the CFD unsteady dataset that was stored to be acoustically exploited through CAA [37] (or IM [33]) exhibited sporadic but rather intense bursts. The latter originated from all the hydrodynamic occurrences (vortices, etc.) convected by the wake downstream of the NLG leg and/or wheels (see the right side of Fig. 14); indeed, when CAA-propagated (resp. IM-extrapolated), a fraction of such hydrodynamic activity was numerically converted into extra (spurious) noise because of the inability of the CAA (resp. IM) stage to resolve accurately enough *all* of the unsteady aerodynamic occurrences, especially over the higher part of the frequency spectrum [34]. It is likely that, in the present case, these spurious noise waves inherited from the CAA conversion of CFD-originated hydrodynamic occurrences [33,37] were interpreted by the sensor array algorithm as additional sources, which were then logically—although abusively—located in the NLG wake region. The observation that only the C19-based numerical outputs were contaminated could be logically explained by the fact that, compared with its F2 star-shaped counterpart, the C19 cross-shaped array was larger, as well as centered slightly downstream of the gear axle (see Fig. 5). These two factors would have made such an array more likely to intercept some of the spurious emissions induced by the wake’s hydrodynamics occurrences.

2. Integrated Power Spectral Density of DAMAS Noise Source Maps

In contrast, one can appreciate how these spurious noise sources appear to have had a rather limited impact on the localization exercise by repeating here the PSD integration previously achieved for the F2

experimental and numerical results (see Sec. IV.A and Fig. 9 above). The left and right sides of Fig. 15 depict the PSD integration of the DAMAS noise source maps plotted in Figs. 11 and 12, respectively. As one can see in the right side of Fig. 15, whatever the larger of the integration area is (global or local), PSD spectra associated with the C19-based CFD-CAA numerical signal exhibit levels that are roughly similar, falling within a 2–3 dB range and matching the PSD of the sole central microphone. This first indicates the relatively low importance of the spurious noise sources, which primarily emerged downstream of the gear (i.e., out of the local integration area). More important, when comparing the locally integrated PSD of the numerical signal to that of its experimental counterpart (see blue curves on the right and left sides of Fig. 15, respectively), one can appreciate how both spectra are very similar—which confirms that the array exploitation of the CFD-CAA calculations were not too corrupted by the spurious noise sources.

Such similarity of the C19-based locally integrated PSDs is depicted in Fig. 10, which compares them to their F2 counterparts as well. Please note that all these PSDs were scaled to a same source-to-array distance of $2R_j$ to account for the distinct locations of both arrays. As one can see, all PSDs are rather similar—with the obvious exception of the F2 experimental one, which emerges because of the spurious effects of the facility (background noise and reverberation; see Sec. IV.A above). When de-biased from such effects of an arbitrary removal of 7 dB over the entire spectrum, this F2-based experimental PSD then collapses almost perfectly with all the other PSDs.

This observation is of importance because it confirms further the coherence of all these noise source localization results and, by

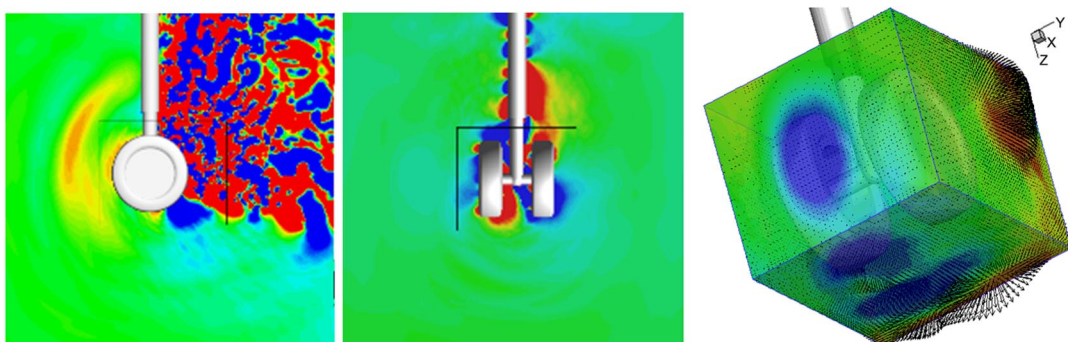


Fig. 14 NLG spurious noise sources induced by the C19 cross-shaped array. Left and center sides: unsteady CFD perturbed field stored on the CFD-CAA interface (black square). Right side: unsteady data plotted over the storage interface at a particular moment where the CFD-CAA interface is crossed by a hydrodynamic burst (black arrows depict the perturbed velocity vectors).

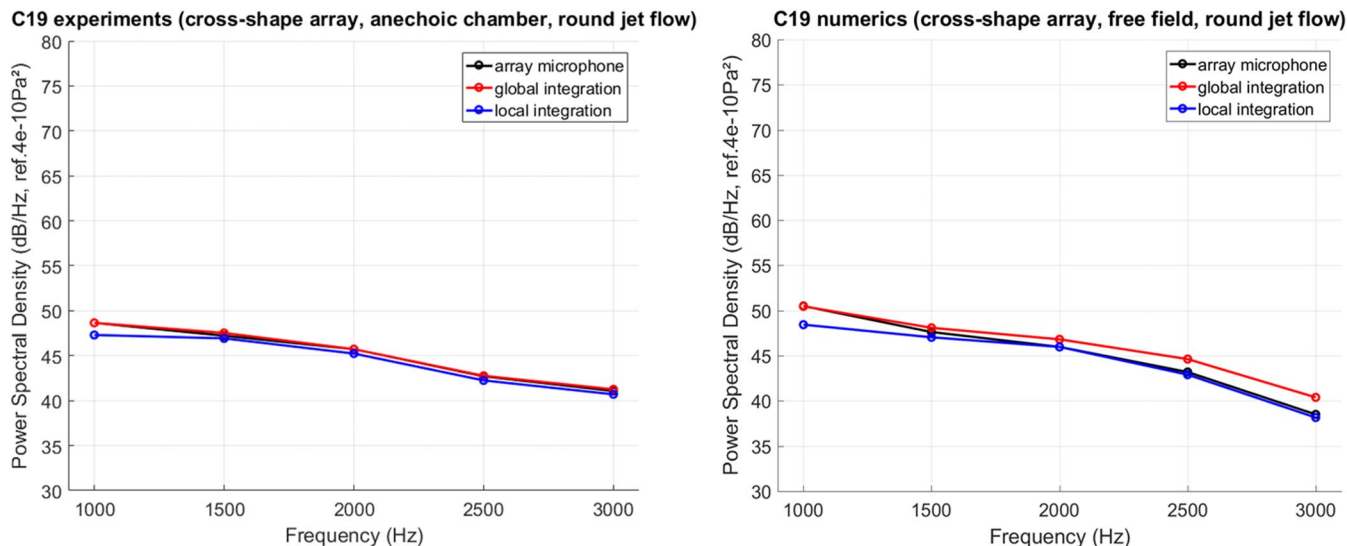


Fig. 15 Integrated levels of the NLG noise source maps obtained through a DAMAS exploitation of either the experimental (left) or the numerical (right) signals associated with the C19-based configuration.

extension, demonstrates that a DAMAS-based localization method can be applied with as much success within a computational context as within an experimental one. This further confirms that the DAMAS approach is compatible with an application to data acquired within noisy environments (e.g., F2), more especially provided that the method is enhanced with proper de-noising and de-reverberation techniques [45,46].

V. Conclusions

The present study addressed noise emission by a simplified nose landing gear (NLG), whose noise sources were localized by the means of two sensor array methods, namely, classical beam forming (CBF) and DAMAS. The latter methods were applied to both experimental and numerical signals that were previously acquired through dedicated aeroacoustics experiments and computations (CFD-CAA hybrid calculations).

The results led to various outcomes of both phenomenological and methodological natures; first, it was shown how these two sensor array methods [and more especially deconvolution approach for the mapping of acoustic sources (DAMAS)] allow discrimination of NLG noise sources, revealing part of their underlying physics (cavity resonances and fluid–structure interactions, in the present case). Then, it was shown how both CBF and DAMAS noise localization techniques can be applied to noise signals of numerical origin as efficiently as to those acquired experimentally. This is an important outcome, as it speaks in favor of a more systematic use of sensor array methods within a computational context. Considering the much higher flexibility that numerical simulation offers compared with experiments (virtual arrays with an unlimited number of microphones, computational setups de-biased from facility installation effects, etc.), this opens the door to many possibilities for numerically investigating aircraft noise source mechanisms.

Here, it is worth noting that, in the wake of this NLG noise source localization exercise, its constitutive elements (e.g., CFD-CAA and experimental signals) will now be disseminated through the Array Analysis Methods workshop sponsored by AIAA and managed by NASA to help the community in benchmarking the signal processing techniques used for localizing aircraft noise sources.

From a more global perspective, the present methodology is currently extended to other problematics, such as the numerical characterization of the acoustic loads and underlying noise sources induced by civil space launchers at lift-off. These follow-on works shall further highlight how advanced simulation and analysis techniques as those used here might help in addressing realistic noise problems in the aerospace industry.

Acknowledgments

Although the present work was funded by ONERA, it took direct benefit from the LAGooN project, which was supported and led by Airbus. In that regard, the authors acknowledge B. Caruelle (Airbus) and E. Manoha (ONERA) for having granted them access to the LAGooN experimental database. The authors thank S. Ben Khelil and G. Cunha (both from ONERA) for having enabled the CFD-CAA hybrid calculations on which the present work relies, respectively, by running the CFD computation and calibrating/postprocessing the CFD storage operations. Finally, the authors acknowledge Dr. Bahr (NASA/LaRC) for his key help in setting up a dedicated benchmark exercise within the Array Analysis Methods workshop on the basis of the outcomes delivered by the present study.

References

- [1] Lazos, B. S., “Surface Topology on the Wheels of a Generic Four-Wheel Landing Gear,” *AIAA Journal*, Vol. 40, No. 12, 2002, pp. 2402–2411. doi:10.2514/2.1608
- [2] Stoker, R., Guo, Y., Streett, C., and Burnside, N., “Airframe Noise Source Locations of a 777 Aircraft in Flight and Comparisons with Past Model-Scale Tests,” *AIAA Paper 2003-3111*, 2003.
- [3] Lazos, B. S., “Reynolds Stresses Around the Wheels of a Simplified Four-Wheel Landing Gear,” *AIAA Journal*, Vol. 42, No. 1, 2004, pp. 196–198. doi:10.2514/1.597
- [4] Remillieux, M. C., Camargo, H. E., Ravetta, P. A., Burdisso, R. A., and Ng, W. F., “Novel Kevlar-Walled Wind Tunnel for Aeroacoustic Testing of a Landing Gear,” *AIAA Journal*, Vol. 46, No. 7, 2008, pp. 1631–1639. doi:10.2514/1.33082
- [5] Manoha, E., Bulté, J., and Caruelle, B., “LAGOON: An Experimental Database for the Validation of CFD/CAA Methods for Landing Gear Noise Prediction,” *AIAA Paper 2008-2816*, 2008.
- [6] Manoha, E., Bulté, J., Ciobaca, V., and Caruelle, B., “LAGOON: Further Analysis of Aerodynamic Experiments and Early Aeroacoustics Results,” *AIAA Paper 2009-3277*, 2009.
- [7] Neuhart, D. H., Khorrami, M. R., and Choudhari, M. M., “Aerodynamics of a Gulfstream G550 Nose Landing Gear Model,” *AIAA Paper 2009-3152*, 2009.
- [8] Van de Ven, T., “Computational and Aeroacoustic Analysis of a 1/4 Scale G550 Nose Landing Gear and Comparison to NASA & UFL Wind Tunnel Data,” *AIAA Paper 2009-3359*, 2009.
- [9] Venkatakrishnan, L., Karthikeyan, N., and Mejia, K., “Experimental Studies on a Rudimentary Four-Wheel Landing Gear,” *AIAA Journal*, Vol. 50, No. 11, 2012, pp. 2435–2447. doi:10.2514/1.J051639
- [10] Reger, R. W., and Cattafesta, L. N., “Experimental Study of the Rudimentary Landing Gear Acoustics,” *AIAA Journal*, Vol. 53, No. 6, 2015, pp. 1715–1720. doi:10.2514/1.J053787

- [11] Souliez, F. J., Long, L. N., Morris, P. J., and Sharma, A., "Landing Gear Aerodynamic Noise Prediction Using Unstructured Grids," *International Journal of Aeroacoustics*, Vol. 1, No. 2, 2002, pp. 115–135. doi:10.1260/147547202760236932
- [12] Li, F., Khorrami, M. R., and Malik, M. R., "Unsteady Simulation of a Landing-Gear Flow Field," AIAA Paper 2002-2411, 2002.
- [13] Hedges, L. S., Travin, A. K., and Spalart, P. R., "Detached-Eddy Simulations over a Simplified Landing Gear," *Journal of Fluid Engineering*, Vol. 124, No. 2, 2002, pp. 413–423. doi:10.1115/1.1471532
- [14] Lockard, D. P., Khorrami, M. R., and Li, F., "Aeroacoustic Analysis of a Simplified Landing Gear," AIAA Paper 2003-3111, 2003.
- [15] Vatsa, V., Lockard, D. P., and Khorrami, M. R., "Application of FUN3D Solver for Aeroacoustics Simulation of a Nose Landing Gear Configuration," AIAA Paper 2011-2820, 2011.
- [16] Xiao, Z., Liu, J., Luo, K., Huang, J., and Fu, S., "Investigation of Flows Around a Rudimentary Landing Gear with Advanced Detached-Eddy-Simulation Approaches," *AIAA Journal*, Vol. 51, No. 1, 2013, pp. 107–125. doi:10.2514/1.J051598
- [17] Deck, S., Gand, F., Brunet, V., and Ben Khelil, S., "High-fidelity Simulations of Unsteady Civil Aircraft Aerodynamics: Stakes and Perspectives. Application of Zonal Detached Eddy Simulation," *Philosophical Transactions Series A (Mathematical, Physical, and Engineering Sciences)*, Vol. 372, No. 2022, 2014, Paper 20130325. doi:10.1098/rsta.2013.0325
- [18] Casalino, D., Ribeiro, A. F. P., Fares, E., and Nölting, S., "Lattice-Boltzmann Aeroacoustic Analysis of the LAGOON Landing-Gear Configuration," *AIAA Journal*, Vol. 52, No. 6, 2014, pp. 1232–1248. doi:10.2514/1.J052365
- [19] Piet, J.-F., and Davy, R., "Airframe Noise Characteristics of a 1/11 Scale Airbus Model," AIAA Paper 1998-2335, 1998.
- [20] Khorrami, M. R., Humphreys, W. M., Lockard, D. P., and Ravetta, P. A., "Aeroacoustic Evaluation of Flap and Landing Gear Noise Reduction Concepts," AIAA Paper 2014-2478, 2014.
- [21] Fleury, V., Bulté, J., Davy, R., and Pott-Pollenske, M., "2D High-Lift Airfoil Noise Measurements in an Aerodynamic Wind Tunnel," AIAA Paper 2015-2206, 2015.
- [22] Howell, G. P., Bradley, A. J., McCormick, M. A., and Brown, J. D., "Dopplerization and Acoustic Imaging of Aircraft Flyover Noise Measurements," *Journal of Sound and Vibration*, Vol. 105, No. 1, 1986, pp. 151–167. doi:10.1016/0022-460X(86)90227-0
- [23] Piet, J.-F., Elias, G., and Lebigot, P., "Localization of Acoustic Source from a Landing Aircraft with a Microphone Array," AIAA Paper 1999-1811, 1999.
- [24] Piet, J.-F., Michel, U., and Bohning, P., "Localization of Acoustic Sources of the A340 with Large Phased Microphone Array During Flight Tests," AIAA Paper 2002-2506, 2002.
- [25] Sijtsma, P., and Stoker, R., "Determination of Absolute Contributions of Aircraft Noise Components Using Fly-Over Array Measurements," AIAA Paper 2004-2958, 2004.
- [26] Fleury, V., and Bulté, J., "Extension of Deconvolution Algorithms for the Mapping of Moving Acoustic Sources," AIAA Paper 2009-3280, 2009.
- [27] Fleury, V., and Bulté, J., "Extension of Deconvolution Algorithms for the Mapping of Moving Acoustic Sources," *Journal of the Acoustical Society of America*, Vol. 129, No. 3, 2011, pp. 1417–1428. doi:10.1121/1.3531939
- [28] Huber, J., Britchford, K., Laurendeau, E., and Long, D., "Understanding and Reduction of Cruise Jet Noise at Model and Full Scale," AIAA Paper 2009-3382, 2009.
- [29] Huber, J., Fleury, V., Bulté, J., and Sylla, A. A., "Understanding and Reduction of Cruise Jet Noise at Aircraft Level," *International Journal of Aeroacoustics*, Vol. 13, No. 1, 2014, pp. 61–84.
- [30] Choudhari, M., Bahr, C. J., Khorrami, M., Lockard, D., Lopes, L., Zawodny, N., Herr, M., Pott-Pollenske, S., Kamruzzaman, M., and Van de Ven, T. et al., "Simulations and Measurements of Airframe Noise: A BANC Workshops Perspective," *Proceedings of NATO STO-MP-AVT-246 Specialists Meeting on Progress and Challenges in Validation Testing for Computational Fluid Dynamics (NATO STO-MP-AVT-246)*, NATO Science and Technology Organization (STO), STO-MP-AVT-246, Bruxelles, Paris, Sept. 2016. doi:10.14339/STO-MP-AVT-246
- [31] Cambier, L., Heib, S., and Plot, S., "The Onera elsA CFD Software: Input from Research and Feedback from Industry," *Mechanics and Industry*, Vol. 14, No. 3, 2013, pp. 159–174. doi:10.1051/meca/2013056
- [32] Redonnet, S., Ben Khelil, S., Bulté, J., and Cunha, G., "Numerical Characterization of Landing Gear Aeroacoustics Using Advanced Simulation and Analysis Techniques," *Journal of Sound and Vibration*, Vol. 403, Sept. 2017, pp. 214–233. doi:10.1016/j.jsv.2017.05.012
- [33] Lopes, L., Redonnet, S., Imamura, T., Ikeda, T., and Cunha, G., "Variability in the Propagation Phase of CFD-Based Noise Prediction," AIAA Paper 2015-2845, 2015.
- [34] Redonnet, S., "Simulation numérique de la propagation acoustique au sein d'écoulements quelconques et de structures solides par résolution des équations d'Euler [Numerical Simulation of Acoustic Propagation within Heterogeneous Flows with Solid Structures through the Solving of Euler Equations]," Ph.D. Thesis, Bordeaux Univ., Pessac, France, Nov. 2001.
- [35] Redonnet, S., Lockard, D. P., Khorrami, M. R., and Choudhari, M. M., "The Non Reflective Interface: An Innovative Forcing Technique for Computational Acoustics Hybrid Methods," *International Journal for Numerical Methods in Fluids*, Vol. 81, No. 1, 2016, pp. 22–44. doi:10.1002/flid.v81.1
- [36] Redonnet, S., and Cunha, G., "An Advanced Hybrid Method for the Acoustic Prediction," *Advances in Engineering Software*, Vol. 88, Oct. 2015, pp. 30–52. doi:10.1016/j.advengsoft.2015.05.006
- [37] Redonnet, S., Cunha, G., and Ben Khelil, S., "Numerical Simulation of Landing Gear Noise via Weakly Coupled CFD-CAA Calculations," AIAA Paper 2013-2068, 2013.
- [38] Brooks, T. F., and Humphreys, W. M., "A Deconvolution Approach for the Mapping of Acoustic Sources (DAMAS) Determined from Phased Microphone Arrays," *Journal of Sound and Vibration*, Vol. 294, Nos. 4–5, 2006, pp. 856–879. doi:10.1016/j.jsv.2005.12.046
- [39] Candel, S., "Etudes Théoriques et Expérimentales de la Propagation Acoustique en Milieu Inhomogène et en Mouvement [Theoretical and Experimental Studies of the Acoustic Propagation within a Moving and Heterogeneous Medium]," Ph.D. Thesis, Paris VI Univ., Paris, 1977.
- [40] Candel, S., "Numerical Solution of Conservation Equations Arising in Linear Wave Theory: Application to Aeroacoustics," *Journal of Fluid Mechanics*, Vol. 83, No. 3, 1977, pp. 465–493. doi:10.1017/S0022112077001293
- [41] Redonnet, S., and Bulté, J., "Numerical Investigation of the Refraction Effects by Jet Flows in Anechoic Wind Tunnels, with Application to NASA/LaRC Quiet Flow Facility," AIAA Paper 2015-3268, 2015.
- [42] Hansen, P. C., *Rank-Deficient and Discrete Ill-Posed Problems: Numerical Aspects of Linear Inversion*, Soc. for Industrial and Applied Mathematics (SIAM), 1998, pp. 99–133. doi:10.1137/1.9780898719697
- [43] Nelson, C., Cain, A. B., Dougherty, R. P., Brentner, K. S., and Morris, P. J., "Application of Synthetic Array Techniques for Improved Simulations of Hot Supersonic Jet Noise," AIAA Paper 2015-0507, 2015.
- [44] Lockard, D. P., Humphreys, W. M., Khorrami, M. R., Fares, E., Casalino, D., and Ravetta, P. A., "Comparison of Computational and Experimental Microphone Array Results for an 18%-Scale Aircraft Model," AIAA Paper 2015-2990, 2015.
- [45] Bulté, J., "Improvement of Acoustic Measurements with an Array of Microphones in Aerodynamic Wind Tunnels," *INTER-NOISE and NOISE-CON Congress and Conference Proceedings, InterNoise06*, Inst. of Noise Control Engineering, Honolulu, HI, 2006, pp. 499–508, <http://www.ingentaconnect.com/content/ince/incecp/2006/00002006/00000007>.
- [46] Bulté, J., "Acoustic Array Measurements in Aerodynamic Wind Tunnels: A Subspace Approach for Noise Suppression," AIAA Paper 2007-3446, 2007.

C. Bailly
Associate Editor